

GOODS-*Herschel*: A population of 24 μm dropout sources at $z < 2$ [★]

Georgios E. Magdis^{1,2}, D. Elbaz¹, M. Dickinson⁴, H.S. Hwang¹, V. Charmandaris^{5,6,7}, L. Armus⁸, E. Daddi¹, E. Le Floch¹, H. Aussel¹, H. Dannerbauer¹, D. Rigopoulou^{2,3}, V. Buat⁹, G. Morrison¹⁰, J. Mullaney¹, D. Lutz¹¹, D. Scott¹², D. Coia¹³, A. Pope¹⁴, M. Pannella¹, B. Altieri¹³, D. Burgarella⁹, M. Bethermin¹⁵, K. Dasyra¹, J. Kartaltepe⁴, R. Leiton¹, B. Magnelli¹¹, P. Popesso¹¹, and I. Valtchanov¹³

¹ Laboratoire AIM-Paris-Saclay, CEA/DSM/Irfu - CNRS - Université Paris Diderot, CE-Saclay, F-91191 Gif-sur-Yvette, France
e-mail: georgios.magdis@astro.ox.ac.uk

² Department of Physics, University of Oxford, Keble Road, Oxford OX1 3RH

³ Space Science & Technology Department, Rutherford Appleton Laboratory, Chilton, Didcot, Oxfordshire OX11 0QX

⁴ National Optical Astronomy Observatory, 950 North Cherry Avenue, Tucson, AZ 85719, USA

⁵ Department of Physics & Institute of Theoretical and Computation Physics, University of Crete, GR-71003, Heraklion, Greece

⁶ IESL/Foundation for Research & Technology-Hellas, GR-71110, Heraklion, Greece

⁷ Chercheur Associé, Observatoire de Paris, F-75014, Paris, France

⁸ Spitzer Science Center, California Institute of Technology, Pasadena, CA.

⁹ Laboratoire d'Astrophysique de Marseille, OAMP, Université Aix-Marseille, CNRS, 38 rue Frédéric Joliot-Curie, 13388 Marseille Cedex 13

¹⁰ Institute for Astronomy, University of Hawaii, Manoa, HI 96822, USA; Canada-France-Hawaii Telescope Corp., Kamuela, HI 96743, USA

¹¹ Max-Planck-Institut für Extraterrestrische Physik (MPE), Postfach 1312, 85741, Garching, Germany

¹² Department of Physics and Astronomy, University of British Columbia, Vancouver, BC V6T 1Z1, Canada

¹³ Herschel Science Centre, European Space Astronomy Centre, Villanueva de la Cañada, 28691 Madrid, Spain

¹⁴ Department of Astronomy University of Massachusetts, LGRT-B 618, 710 North Pleasant Street, Amherst, MA 01003

¹⁵ Univ Paris-Sud, Laboratoire IAS, UMR8617, 91405, Orsay Cedex, France; CNRS, Orsay, 91405, France

Preprint online version: June 15, 2018

ABSTRACT

Using extremely deep PACS 100- and 160 μm *Herschel* data from the GOODS-*Herschel* program, we identify 21 infrared bright galaxies previously missed in the deepest 24 μm surveys performed by *Spitzer*/MIPS. These MIPS dropouts are predominantly found in two redshift bins, centred at $z \sim 0.4$ and ~ 1.3 . Their S_{100}/S_{24} flux density ratios are similar to those of local (ultra-) luminous infrared galaxies (LIRGs and ULIRGs), whose silicate absorption features at 18 μm (at $z \sim 0.4$) and 9.7 μm (at $z \sim 1.3$) are shifted into the 24 μm MIPS band at these redshifts. The high- z sub-sample consists of 11 infrared luminous sources, accounting for $\sim 2\%$ of the whole GOODS-*Herschel* sample and putting strong upper limits on the fraction of LIRGs/ULIRGs at $1.0 < z < 1.7$ that are missed by the 24 μm surveys. We find that a $S_{100}/S_{24} > 43$ colour cut selects galaxies with a redshift distribution similar to that of the MIPS dropouts and when combined with a second colour cut, $S_{16}/S_8 > 4$, isolates sources at $1.0 < z < 1.7$. We show that these sources have elevated specific star formation rates (sSFR) compared to main sequence galaxies at these redshifts and are likely to be compact starbursts with moderate/strong 9.7 μm silicate absorption features in their mid-IR spectra. *Herschel* data reveal that their infrared luminosities extrapolated from the 24 μm flux density are underestimated, on average, by a factor of ~ 3 . These *silicate break* galaxies account for 16% (8%) of the ULIRG (LIRG) population in the GOODS fields, indicating a lower limit in their space density of $2.0 \times 10^{-5} \text{ Mpc}^{-3}$. Finally, we provide estimates of the fraction of $z < 2$ MIPS dropout sources as a function of the 24-, 100-, 160-, 250- and 350 μm sensitivity limits, and conclude that previous predictions of a population of silicate break galaxies missed by the major 24 μm extragalactic surveys have been overestimated.

Key words. galaxies: active – galaxies: evolution – galaxies: formation – galaxies: starburst – infrared:galaxies

1. Introduction

Accurate measurement of star formation rates (SFR) is a key ingredient for studying galaxy evolution and deriving the census of the star formation activity, both in the distant and in the local universe. To this end, it has been shown that the contribution of luminous infrared galaxies (with infrared luminosities $L_{\text{IR}} > 10^{11} L_{\odot}$) to the star formation density is progressively rising as we look back in cosmic time, at least up to $z \sim 2$. Indeed, although

they were found to be rare in the local Universe and to account for only $\sim 5\%$ of the total infrared energy emitted by galaxies at $z \sim 0$ (Soifer et al. 1991, Kim & Sanders 1998), LIRGs and ULIRGs ($L_{\text{IR}} > 10^{12} L_{\odot}$), dominate the SFR density at $z \sim 1-2$, accounting for 70% of the star formation activity at these epochs (Papovich et al. 2004, Le Floch et al. 2005, Caputi et al. 2007).

The study of infrared sources was greatly facilitated by the advent of the Spitzer Space Telescope (*Spitzer* Werner et al. 2004). Extragalactic surveys carried out using the MIPS 24 μm band on-board *Spitzer* confirmed the strong evolution of these sources first indicated by infrared and submillimeter observations using *ISO* and SCUBA, respectively (Blain et al. 1999a,

[★] *Herschel* is an ESA space observatory with science instruments provided by European-led Principal Investigator consortia and with important participation from NASA.

Elbaz et al. 1999, Serjeant et al. 2001, Dole et al. 2001). Such surveys are believed to detect the bulk of the dusty star forming galaxies up to $z \sim 2$. However there are two important caveats. The first is that the conversion of 24 μm flux densities to total L_{IR} (and therefore SFR) is subject to large uncertainties, as it relies on extrapolations that strongly depend on the assumed spectral energy distribution (SED) libraries (Chary & Elbaz 2001; Lagache et al. 2003; Dale & Helou 2002). The second comes from the prominent emission and absorption features between 3- and 19 μm in the spectra of star forming galaxies that parade through the 24 μm band at various redshifts.

A large number of studies using the Infrared Spectrograph (IRS, Houck et al. 2004) have revealed that the vast majority of local LIRGs and ULIRGs exhibit a broad silicate absorption feature centred at 9.7 μm with silicate optical depths ranging from $\tau_{9.7} \sim 0.4$ to $\tau_{9.7} \geq 4.2$ (Brandl et al. 2006; Armus et al. 2007; Pereira-Santaella et al. 2010). Furthermore, using a sample of local ULIRGs, Desai et al. (2007) found strong PAHs and prominent silicate absorption in the H II and LINER sources and weak PAHs and silicate absorption in Seyferts, suggesting that ULIRGs with strong PAHs but weak silicate absorption are rare. Similar features have been observed in the mid-IR spectra of high- z galaxies (Higdon et al. 2004, Houck et al. 2005). For example, Menéndez-Delmestre et al. (2009) and Farrah et al. (2008) report a median $\tau_{9.7} \sim 0.31$ for a sample of submillimetre galaxies (SMGs) and IRAC selected ULIRGs respectively, while Sajina et al. (2007) found deeper silicate absorption features ($\tau_{9.7} > 1.1$) in a sample of $z \sim 2$ radio-loud galaxies. Although for LIRGs and ULIRGs the identification and measurement of the silicate optical depths is straightforward, this is not the case for normal galaxies ($L_{\text{IR}} < 10^{10} L_{\odot}$), as for the latter, it is difficult to discriminate between moderate PAH emission superimposed on a silicate-absorbed continuum and strong PAH features with a relatively weak underlying continuum (Smith et al. 2007).

Whatever its origin, the existence of this broad dip in the mid-IR spectra of star forming galaxies 10 μm could be of particular importance for galaxies in the redshift range of $1 < z < 1.8$. At these redshifts the 24 μm filter samples this part of the spectrum and sources with such features would appear faint at 24 μm or even be undetected in this band (depending on the depth of the 24 μm data). A second broad dip that is common in the spectra of star forming galaxies is caused by another silicate absorption feature at 18 μm . This feature would have a similar effect for sources at $0.2 < z < 0.6$.

The impact of these features on the mid-IR colours as a function of redshift were presented in detail by Takagi & Pearson (2005), who predicted a population of infrared luminous galaxies at $z \sim 1.5$ which, due to strong absorption at 9.7 μm , are not detected in the 24 μm band. Subsequent studies that focussed on the search for such silicate absorbed systems employed the 16 μm IRS peak-up image. Kasliwal et al. (2005) suggested that such objects account for more than half of all the sources at $z \sim 1-2$ predicted by various models. It has also been proposed that the mid-IR colour anomalies introduced by the silicate absorption feature can serve as a redshift indicator for dusty infrared luminous galaxies at $z \sim 1.5$ (Charmandaris et al. 2004, Teplitz et al. 2011, Armus et al. 2007). Similar claims have also been presented by Pearson et al. (2010), using the AKARI IRC L18W to MIPS24 band colour. These studies raised concerns about a possible bias introduced by the 24 μm selection, in the sense that a significant fraction of $z \leq 2$ LIRGs and ULIRGs could remain undetected in 24 μm surveys. However, with little or no information about the far-IR part of the spectrum, these studies were

subject to large extrapolation and hence suffered from large uncertainties.

With the successful launch of the Herschel Space Observatory (*Herschel*, Pilbratt et al. 2010), we now have access to wavelengths that directly probe the peak of the far-IR emission of high- z galaxies and are in a position to measure with unprecedented accuracy their bolometric output. Deep *Herschel* extragalactic surveys can be used to determine the accuracy of our extrapolations of the far-IR properties of high- z galaxies as well as test previous claims that 24 μm surveys miss a population of $z < 2$ LIRGs and ULIRGs (24 μm dropouts). In this paper, we use the deepest *Herschel* observations to date, as part of the GOODS-*Herschel* (GOODS-H) program (PI D. Elbaz), covering both the north and the south part of the GOODS fields (GOODS-N and GOODS-S respectively), (Dickinson et al. 2003, Giavalisco et al. 2004), to search for such sources. In Section 2 we present the *Herschel* data, introduce the GOODS-H sample of galaxies, and identify 24 μm dropout sources, i.e., sources detected in the PACS bands but not at 24 μm . In Section 3 we investigate the properties of this population, while in Section 4 we extend our study to the whole GOODS-H sample. Finally in Section 5 we provide estimates of the fraction of $z < 2$ MIPS dropout sources as a function of the 24 μm , 100 μm and 160 μm sensitivity limits and summarize our results.

2. Herschel data and sample selection

Herschel observations were obtained as part of the open time key program GOODS-H (PI D. Elbaz). The full $10' \times 16'$ GOODS-N field was imaged with the PACS (Poglitsch et al. 2010) and SPIRE (Griffin et al. 2010) instruments at 100, 160 μm (PACS) and 250, 350, 500 μm (SPIRE). The total observing time was 124.6 hours ($\sim 2.5\text{h}$ / sky position) and 31.1 hours for PACS and SPIRE respectively. Similarly a $7' \times 7'$ part of the GOODS-S field was observed by PACS over a total of 264 hours ($\sim 15\text{h}$ / sky position). Observations of both fields were carried out by adopting the intermediate speed ($20''\text{s}^{-1}$) scan-map mode. Both PACS and SPIRE data were processed through the standard *Herschel* reduction pipeline, version 6.0.3, within the HCSS environment. Additionally, we employed custom procedures aimed at removing of interference patterns, tracking anomalies, re-centering positional offsets, and mapping. A full description of the data reduction procedures will be given in a companion paper (Leiton et al. 2011 in prep).

2.1. Prior based Source extraction; The GOODS-H sample

Given the large beam size of the *Herschel* bands, (FWHM $\sim 6.7'', 11.2'', 18.0'', 25.0'', 36.0''$ for PACS 100- and 160 μm and SPIRE 250, 350 and 500 μm), a common approach to performing source extraction has been a guided extraction using priors. Here we will give a brief summary of the procedure as an extensive description of the method is given in Elbaz et al. (2011). Source extraction and photometry were obtained from point source fitting at prior positions defined by 24 μm sources with fluxes brighter than $S_{24} \sim 20 \mu\text{Jy}$ for the 100 μm maps and down to $S_{24} \sim 30 \mu\text{Jy}$ for the 160 μm and 250 μm maps. For the other two SPIRE bands, a secondary criterion was needed, as the 24 μm sources were far too numerous and would lead to an over-deblending of the actual sources. Hence, only sources with $S/N > 2$ at 250 μm were considered as priors for the longer wavelength SPIRE bands. This choice was optimized by Monte Carlo (MC) simulations to avoid artificial over-deblending of a source, but also to give clean residual maps. Flux uncertainties

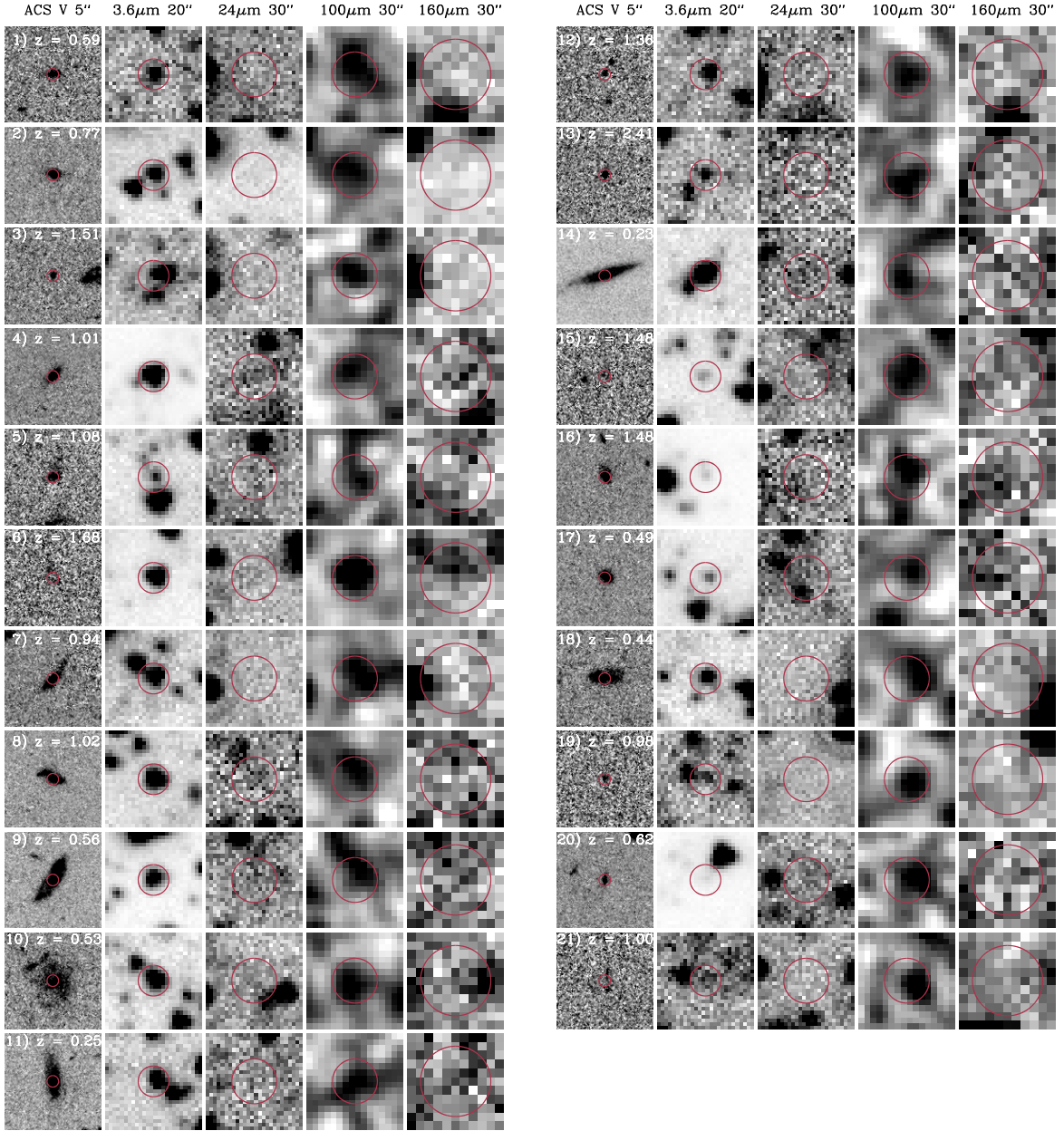


Fig. 1. ACS V -band ($5'' \times 5''$), IRAC $3.6\mu\text{m}$ ($20'' \times 20''$), MIPS $24\mu\text{m}$ ($30'' \times 30''$), and PACS 100-, $160\mu\text{m}$ ($30'' \times 30''$) cut-out images of the $24\mu\text{m}$ dropout sources from our sample. The red circles are centred at the IRAC $3.6\mu\text{m}$ positions of the sources and their diameter corresponds to the FWHM at each band. The size of each image is denoted on the top of each column.

were based on local estimates of the background noise at the position of the sources from residual images produced after subtracting detected sources, while global noise estimates for the maps were derived from Monte Carlo simulations. This used artificial sources injected into the *Herschel* maps and source extraction performed in the same manner as for the real sources. The dispersion between input and recovered fluxes provides a secure estimate of the completeness and the noise properties of the map. The two noise estimates were found to be in good agreement.

To construct the GOODS-H sample, we considered sources with flux densities down to 3σ in the PACS bands, i.e. 1.0 and 2.6 mJy (0.7 and 2.6 mJy) at 100 and $160\mu\text{m}$ in GOODS-N

(GOODS-S). For the GOODS-N sample, where SPIRE data are available we also considered sources down to the 5σ detection limit, i.e. 6.3, 7.1, and 15.0 mJy at 250, 350 and $500\mu\text{m}$, respectively. The choice of a higher S/N cut for the SPIRE catalogues was dictated by the larger beam size and the confusion noise that significantly affects the SPIRE observations (for more details see Elbaz et al. 2011). *Herschel* catalogs were then matched with the existing multi-wavelength data of the GOODS team to create a multi-band merged catalogue of GOODS galaxies including *HST ACS BVis, J, K, IRAC, Spitzer MIPS 24 and 70 μm , Herschel PACS 100 and $160\mu\text{m}$, and Herschel SPIRE 250, 350 and $500\mu\text{m}$. Among our sources, 65% have secure spectroscopic redshifts, while for the rest, we use the reliable compilation of*

photometric redshifts by Le Borgne et al (2009). Hereafter we will refer to this sample as the GOODS-H sample.

2.2. Blind source extraction; The 24 μm dropout sample

Since the main aim of this work is to investigate whether *Herschel* observations reveal a population of galaxies that were previously missed by 24 μm surveys, we also performed blind source extraction in the two PACS bands using *Starfinder*, a point spread function (PSF) fitting code (Diolaiti et al. 2000). We first extracted PSF profiles from the final science maps that were used to perform source extraction. Aperture corrections were derived based on calibration observation of the asteroid Vesta, while the flux uncertainties were derived based both on the error maps and Monte Carlo simulations, as described above. Monte Carlo simulations were also employed to obtain the level of completeness and the fraction of spurious sources. Both the derived fluxes and the noise properties of the maps are in good agreement with those obtained by the prior based source extraction. Finally, a critical parameter in *Starfinder* is the *correlation threshold* (ct), a measure of the similarity between the PSF used for source extraction and the profile of the extracted source, with ct=1 corresponding to identical profiles. MC simulations indicate that high ct values result in catalogs immune to spurious detections but with lower completeness levels. Similarly lower ct values correspond to higher completeness but also to higher fractions of spurious sources. For our blind catalogs we consider sources with flux densities above the 4σ detection limit at each band and ct > 0.67, for which the fraction of spurious sources is < 3%.

In principle, our aim was to find sources detected in either of the PACS bands but undetected at 24 μm . Therefore, we first matched the PACS 100- and 160 μm blind catalogs with the MIPS24 μm sample down to $S_{24} \sim 20 \mu\text{Jy}$ (3σ), i.e. the one that served as a pool for the prior based source extraction, starting from the longest wavelength available and using search radii of 7" and 11" respectively. Sources with 24 μm counterparts were omitted while the rest were matched to the IRAC 3.6 μm catalogue and subsequently to the master GOODS multi-bands catalogue described in the previous section. We also performed photometry in the 24 μm maps at the position of the PACS sources to ensure that there is no 24 μm source at this position, possibly missing from the 24 μm catalogue. We calculated the corrected Poissonian probability that an association of a PACS source within the search radius is a chance coincidence (see Downes et al. 1986) and all sources were found to have a robust ($p < 0.05$) 3.6 μm counterpart. We also note that flux boosting due to insufficient de-blending, which is the main caveat of blind source extraction, should not, by definition, be an issue for the 24 μm dropout sample. All sources were also inspected by eye and a quality flag was attributed to them. In particular, sources with multiple IRAC counterparts within the PACS beam and sources close to bright objects in the PACS bands were flagged as low quality sources. The final sample consists of 21 MIPS dropout sources, all detected at 100 μm and two at 160 μm , accounting for $\sim 2\%$ of the total sources detected in the PACS bands. Hence, we find that even at the confusion limit of the 100- and 160 μm passbands (0.7- and 2.6 mJy at a 3σ level), 98 % of the *Herschel* sources possess a robust 24 μm counterpart brighter than 20 μJy . The 21 MIPS dropout sources are shown in Fig. 1 where we present cut-out images at several bands.

3. 24 μm dropout sources

The small number of 24 μm dropouts indicates that the vast majority of PACS sources do have a 24 μm counterpart. In other words, the “normal” SED behaviour of galaxies in the GOODS sample is the one where the relative sensitivity at 24 μm overpowers that of the PACS bands. In Fig. 2 (left) we plot the flux density at 24 μm over that at 100 μm for the whole GOODS-H sample, as well as for the dropout sources and see that the latter depart from the general trend and are relatively faint at 100 μm . We also note that similarly to the MIPS dropouts, some sources with 24 μm detection tend to exhibit redder S_{100}/S_{24} colours than the bulk of the population while they span a wide range of S_{24} . Here we will study the origin of the departure of the MIPS dropouts from the bulk of the GOODS-H sample and our investigation will be driven by their property that intrigued our interest in the first place i.e. their unusual S_{100}/S_{24} colour.

3.1. Far-IR properties

The total infrared luminosity ($L_{\text{IR}} = L_{8-1000\mu\text{m}}$) of galaxies in the sample was determined from the 100 μm flux density using the templates of (Chary & Elbaz 2001, CE01) and Dale & Helou (2002) (DH02). Despite the lack of data points at longer wavelengths, we note that the monochromatic derivations of total IR luminosities from the 100 μm flux density tend to be robust up to $z \sim 1.5$ (Elbaz et al. 2010). For the two sources with 160 μm detection L_{IR} was determined from the best fit of the two PACS points, using the whole library of SED templates from CE01 independently of their luminosity (i.e. allowing normalization of all SEDs to the observations) as well as the DH02 templates. The derived luminosities range from 8×10^9 to $2 \times 10^{12} L_{\odot}$, with 11 of the MIPS dropout sources having $L_{\text{IR}} > 10^{11} L_{\odot}$, belonging to the class of luminous infrared galaxies. To illustrate the completeness of our sample in terms of L_{IR} , we plot the L_{IR} for the GOODS-H sample, as well as for the drop-out sources as a function of redshift, along with the corresponding detection limits at 100 μm and 24 μm (Fig.2 middle). Furthermore, In Fig. 2 (right), we also plot the S_{100}/S_{24} colour as a function of L_{IR} as derived from the *Herschel* data, both for the whole GOODS sample as well as for the MIPS dropouts (crosses with arrows). For the latter we compute lower limits to S_{100}/S_{24} assuming the 3σ detection limit of the 24 μm maps. The points are also colour-coded based on their redshift. We see that 24 μm dropouts have L_{IR} values similar to that of the whole GOODS-H sample (for a given redshift), while they exhibit significantly higher S_{100}/S_{24} colours for the whole range of luminosities. As we discussed above, L_{IR} scales with S_{100} . Hence, given the richness of features in the rest frame MIR emission (i.e. Armus et al. 2007), it is more likely that the dropouts have a suppressed S_{24} emission rather than an excess at S_{100} when compared to the rest of the GOODS-H sample. In what follows we investigate the origin of this S_{24} deficit.

3.2. S_{100}/S_{24} colour and redshift distribution

We wish to examine whether the MIPS dropout sources tend to be found at specific redshifts. We note that nine sources have spectroscopic redshift, while for the rest we adopt the photometric redshifts derived by the GOODS team. It appears that 24 μm dropouts are distributed in two redshift bins, one centred at $z \sim 0.4$ and one at $z \sim 1.3$ (Fig. 3). This bimodality is verified by a KMM test (Ashman et al. 1994) at a 4.3σ confidence level. Therefore, it seems that our sample is populated by low- z ($0.2 <$

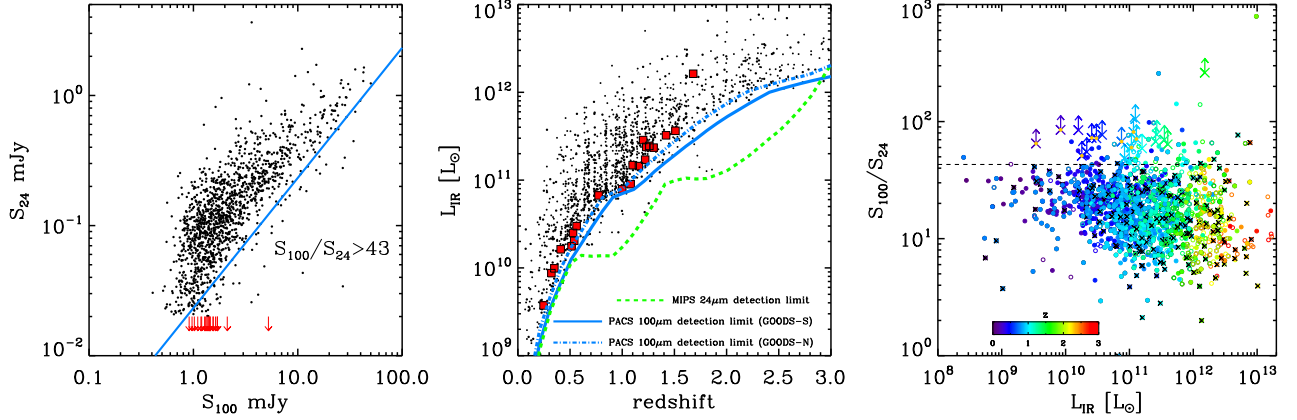


Fig. 2. Left: S_{24} vs S_{100} flux densities for the whole GOODS-H sample (black circles) as well as for the 24 μ m dropout sources (red arrows). For the dropouts we consider a 3σ upper limit for the S_{24} . Dropouts as well as some 24 μ m detected sources tend to depart from the bulk of the GOODS-H population, exhibiting redder S_{100}/S_{24} colours. The cyan line corresponds to $S_{100}/S_{24} = 43$. As discussed later in the paper, sources with $S_{100}/S_{24} > 43$ are classified as *silicate-break* galaxies. Middle: Detection limits as a function of redshift for the GOODS-N and GOODS-S PACS 100 μ m and MIPS 24 μ m observations. Red squares correspond to the dropout sources. Right: S_{100}/S_{24} as a function of L_{IR} as derived by *Herschel* for the whole GOODS-H sample (circles) and lower limits for the 24 μ m dropouts (arrows). Both samples are colour coded based on their redshift. Sources with a black cross are AGNs based on their X-ray emission. Filled symbols denote sources in the GOODS-H sample with spectroscopic redshifts while open symbols sources with photometric redshift. Similarly, yellow circles on top of the arrows indicate that a spectroscopic redshift is available for that 24 μ m dropout source. The horizontal black dashed line corresponds to $S_{100}/S_{24} = 43$.

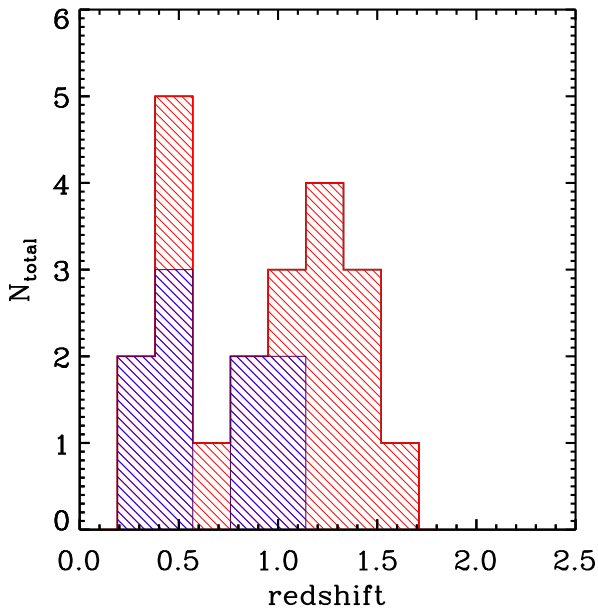


Fig. 3. Redshift distribution of sources in the MIPS dropout sample. A KMM test suggests a bimodal distribution centred at $z \sim 0.4$ and $z \sim 1.3$. Blue shadowed area corresponds to the distribution of sources with spectroscopic redshift.

$z < 0.6$) and high- z ($0.9 < z < 1.7$) sources. Similarly to Fig. 2, we now plot the S_{100}/S_{24} colour as a function of redshift (Fig. 4). In this figure we also overplot the S_{100}/S_{24} colour as a function of redshift for a number of local LIRGs/ULIRGs based on their observed SED as constructed by IRS observations of their mid-IR spectrum (Armus et al. 2007) and *IRAS* observations of their far-IR emission (Rieke et al. 2009). The observed templates were chosen to span a wide range of L_{IR} and silicate optical depths ($\tau_{9.7}$) and their full SEDs are presented in Fig. 5, in order of increasing $\tau_{9.7}$. The $\tau_{9.7}$ measurements are adopted from Armus et al. (2007) (Arp200, NGC 22491), Pereira-Santaella et al. (2010) (ESO 320-G030, NGC 2369, Zw 049.057, NGC 3256) and da

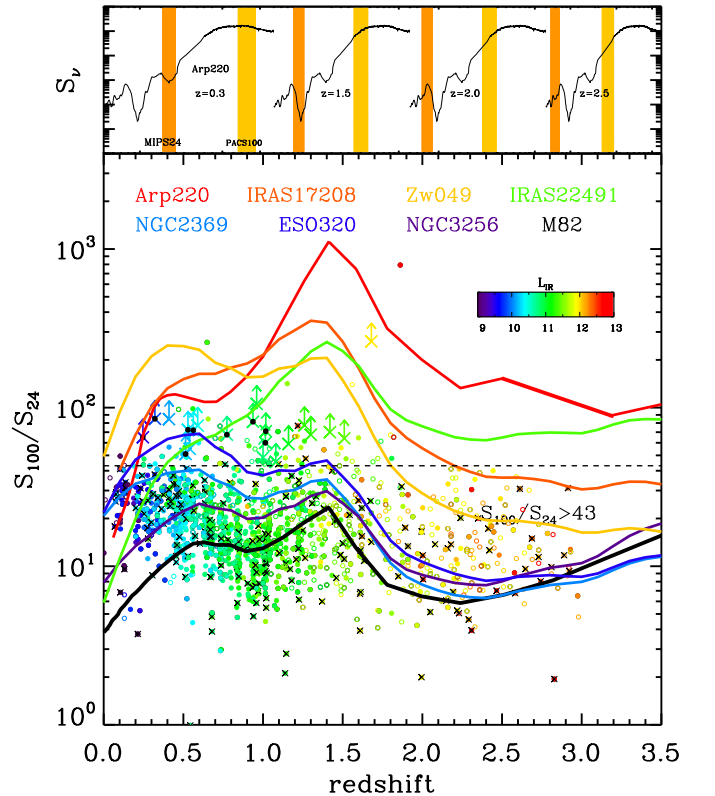


Fig. 4. S_{100}/S_{24} as a function of redshift for the whole GOODS-H sample (circles) and lower limits for the 24 μ m dropouts (arrows). Both samples are colour coded based on their L_{IR} . Sources with a black cross are AGNs based on their X-ray emission. Filled symbols denote sources in the GOODS-H sample with spectroscopic redshift, while open symbols are sources with photometric redshift. Similarly, black circles on top of the arrows indicate that a spectroscopic redshift is available for that MIPS dropout source. Solid lines correspond to different observed SEDs of local LIRGs/ULIRGs (see Fig. 5) and horizontal black dashed line to $S_{100}/S_{24} = 43$. The top panel shows the SED of Arp220 at various redshifts along with the MIPS 24- and PACS 100 μ m bands.

Cunha et al. (2010) (IRAS 17128). On the top of Fig. 4 we also show the SED of Arp220, along with the 24- and 100 μm bands at several redshifts. It is evident that the S_{100}/S_{24} colour of the templates varies significantly as a function of redshift, mainly due to the presence of the silicate absorption features at 9.7- and 18 μm that enter the MIPS 24 μm filter at $z \sim 1.4$ and ~ 0.3 respectively. We also note a wide range of S_{100}/S_{24} colours for a given redshift, indicative of different amounts of extinction as well as different dust temperatures. Indeed, Fig. 5 suggests a weak trend for SEDs of sources with deeper silicate absorption to peak at shorter wavelengths. Therefore, the S_{100}/S_{24} values increase because S_{24} is suppressed by the silicate absorption features, but are also further elevated due to higher dust (big grain) temperatures and hence S_{100} values.

Looking back at Fig. 4, we see that 24 μm dropouts, although they have higher S_{100}/S_{24} values when compared to the whole sample, exhibit colours that are consistent with those of local star formation dominated ULIRGs/LIRGs. The fact that the redshift distribution of 24 μm dropouts peaks at redshifts where the 9.7- and 18 μm silicate absorption features enter the 24 μm band indicates that these sources could have moderate/strong silicate absorption features. On the other hand, the high S_{100}/S_{24} ratio could also result from lower levels of observed dust continuum emission at 24 μm , but as we will see later that our data disfavour this scenario. In any case, all 24 μm dropouts fall within the envelope defined by the templates, so they form an extreme rather than an extraordinary population of star forming galaxies. We also note that none of the drop-out sources have an X-ray detection or meet the criteria for a power-law AGN.

Previous studies have attempted to identify infrared luminous sources that are undetected at 24 μm by combining 16 μm IRS peak-up imaging with 24 μm data (Kasliwal et al. 2005, Teplitz et al. 2011) and following an approach similar to the one presented in this work. They searched for sources at $z \sim 1.3$, that are faint at 24 μm , due to the shift of the silicate absorption features into the MIPS band, but bright at 16 μm due to 7.7 μm PAH emission, concluding that sources with $S_{16}/S_{24} > 1.2$ tend to be found at $z > 1.1$. They also investigated the S_{16}/S_{24} colours of several local LIRGs/ULIRGs and report an average ratio of $\sim 1-2$ for galaxies with strong silicate absorption features. From our 24 μm dropout sample, none of the sources are detected at 16 μm down to the 3σ detection limit ($S_{16} \sim 40 \mu\text{Jy}$ for GOODS-N and $\sim 65 \mu\text{Jy}$ for GOODS-S, Teplitz et al. 2011). Apart from the fact that some of our sources are outside the area covered by the IRS peak-up image in the GOODS fields, the non-detection of the rest of the sources at 16 μm is somewhat expected from the discussion above. Even if we adopt a $S_{24} = 20 \mu\text{Jy}$ for all sources in the sample and assume a $S_{16}/S_{24} = 2.0$ (Arp220 case, Armus et al. 2007) then our sources should only be marginally detected at the depth of the 16 μm GOODS maps.

3.3. A $z \sim 1.68$ ULIRG, missed by MIPS

Although the study of the properties of individual 24 μm dropout sources is beyond the scope of this study, here we wish to have a closer look at a specific source for which, *Herschel* data indicate an infrared luminosity $L_{\text{IR}} > 10^{12} L_{\odot}$. This is the only source in our high- z sample with detection at 100 μm ($S_{100} = 5.2 \pm 0.42 \text{ mJy}$), 160 μm ($S_{160} = 6.9 \pm 1.1 \text{ mJy}$) and at 250 μm . The source also has also a $\sim 6\sigma$ detection at the GOODS-N VLA 1.4GHz map ($S_{1.4} = 32.1 \pm 5.1 \mu\text{Jy}$). Unfortunately, the source is out of the area covered by IRS 16 μm peak-up imaging. Cut out images of this galaxy are shown in the sixth row of Fig. 1. To derive the far-IR properties of the source we fit the observed

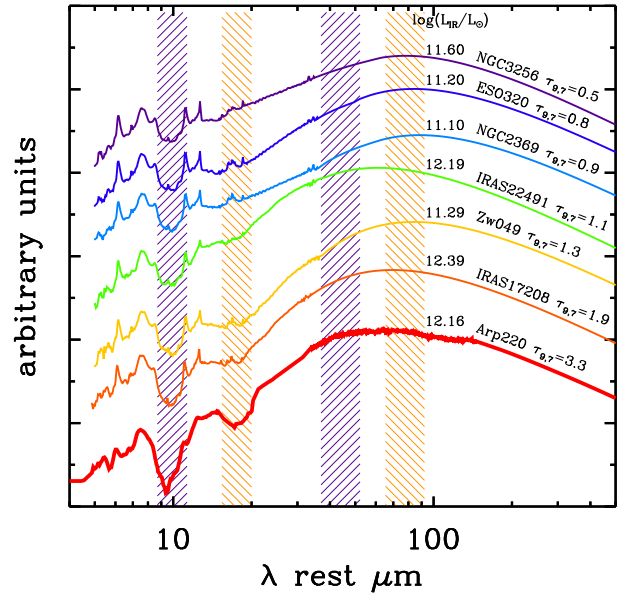


Fig. 5. A large range of rest frame SEDs of local ULIRGs and LIRGs, presented in increasing order of silicate optical depth. The mid-IR part is the IRS spectrum (Armus et al. 2007), while the far-IR comes from Rieke et al. (2009) templates. Blue (orange) stripes correspond to MIPS 24- and PACS 100 μm bands at $z=1.3$ (0.3)

Herschel points with CE01 models, but also with a range of observed SEDs of local ULIRGs, described in the previous section. The observed multi-band photometry, together with the best fit SEDs are shown in Fig. 6.

The derived infrared luminosity of the source is $L_{\text{IR}} = 1.3-1.6 \times 10^{12} L_{\odot}$ (depending on the assumed SED), but it is evident that only templates with a strong silicate absorption feature at 9.7 μm can reproduce the non-detection down to $20 \mu\text{Jy}$ at 24 μm . Fitting the optical part of the SED with BC03 models, yields a stellar mass of $8.9 (\pm 0.5) \times 10^{10} M_{\odot}$, while based on the β slope of the UV spectrum we derive a reddening $E(B-V) = 2.1$, consistent with a heavily obscured source. Assuming a Salpeter IMF and the Kennicutt (1998) relation we convert the *Herschel*-based L_{IR} to star formation rate and derive $\text{SFR} \sim 280 M_{\odot} \text{ yr}^{-1}$. Similarly, we convert the radio flux to L_{IR} (Condon 1992) and subsequently to SFR, finding that the two estimates are in perfect agreement ($\text{SFR}_{\text{radio}} = 300 \pm 32 M_{\odot} \text{ yr}^{-1}$). The source is not detected in X-rays and exhibits the 1.6 μm stellar bump, indicating that there is no near-to-mid-IR evidence for the presence of an AGN. The above analysis suggests that this is a heavily obscured starburst galaxy with no signs of AGN activity. Although unique in our sample, this galaxy raises the question of how many such objects we might have missed in the pre-*Herschel* era and what would be their contribution to the cosmic SFR density. A detailed discussion on this point will be presented in section 5.

4. Silicate-break galaxies

So far, we have demonstrated that *Herschel* data have revealed a small but interesting class of infrared luminous galaxies, which are undetected at 24 μm . The main characteristic of these sources is their atypically red S_{100}/S_{24} colour. Furthermore, Fig. 2 (left), reveals that sources with S_{100}/S_{24} colours similar to those of the dropouts can be found among sources with 24 μm detection. In

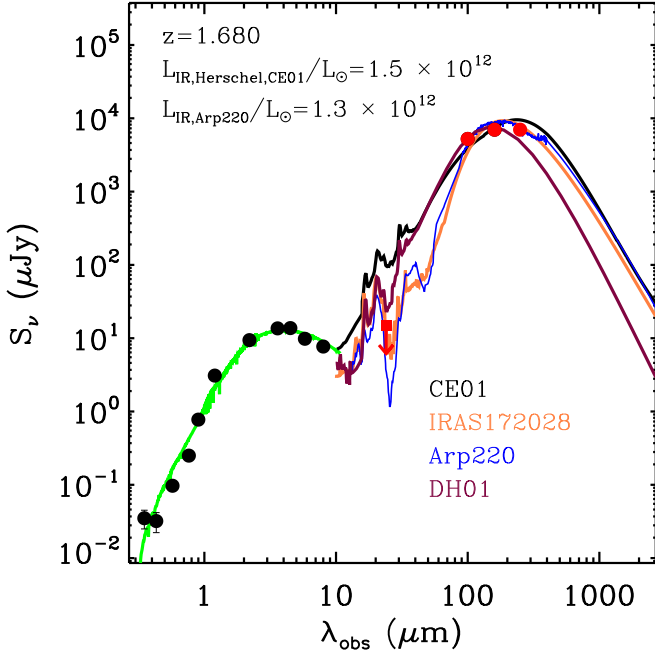


Fig. 6. The SED of a dropout at $z = 1.68$, detected in both the 100- and 160 μm bands, although missed at 24 μm . The optical part is overlaid with the best fit BC03 model (green line) and the infrared part with a range of observed and model SEDs. The red square denotes the upper limit at 24 μm . Cut-out images of the source are shown in Fig. 1, 6th row.

what follows we extend our study to the whole GOODS-H sample, searching for such objects.

To select them, we adopt a cut off, $S_{100}/S_{24} > 43$, that corresponds to the bluest lower limit among the MIPS dropout sample and the colour of the local LIRG ESO320 shifted at $z = 1.4$. In Fig. 7 we plot the redshift distribution of sources with $S_{100}/S_{24} > 43$ (excluding the dropouts), finding that it bears a remarkable resemblance to that of the 24 μm dropouts in Fig. 3. Indeed, a K-S test reveals that there is no significant difference between the two samples with a p value of 0.61. In contrast, we find that the sample has a redshift distribution quite different than that of the whole GOODS-N sample (Fig. 7, top panel) at a confidence level of $>97.5\%$. Similar to the dropout sample, sources with $S_{100}/S_{24} > 43$ exhibit a bimodal redshift distribution at the 3.5σ level, centred at $z \sim 0.48$ and ~ 1.3 . Therefore, in what follows, we suggest that the S_{100}/S_{24} colour could serve as redshift indicator.

4.1. S_{100}/S_{24} colour as a redshift indicator.

In the pre-*Herschel* era, there were several attempts to use anomalous MIR colours as a crude redshift indicator. These studies mainly employed the 16 μm IRS peak-up imaging and proposed that a blue S_{16}/S_{24} colour would peak in a narrow redshift bin, $1.0 < z < 1.8$ (Armus et al. 2007, Teplitz et al. 2011), as well as being useful for selecting infrared luminous galaxies in this redshift bin that were undetected by the 24 μm band. The main idea behind this criterion is that at these redshifts the 9.7 μm silicate absorption feature enters in the 24 μm passband, while the strong PAH emission features at 6.2- and 7.7 μm are shifted into the 16 μm band, producing a distinctive blue S_{16}/S_{24} colour. For example, Kasliwal et al. (2005) used a $S_{16}/S_{24} > 1.2$ ratio to select objects at $1.1 < z < 1.6$, and called them “silicate-break

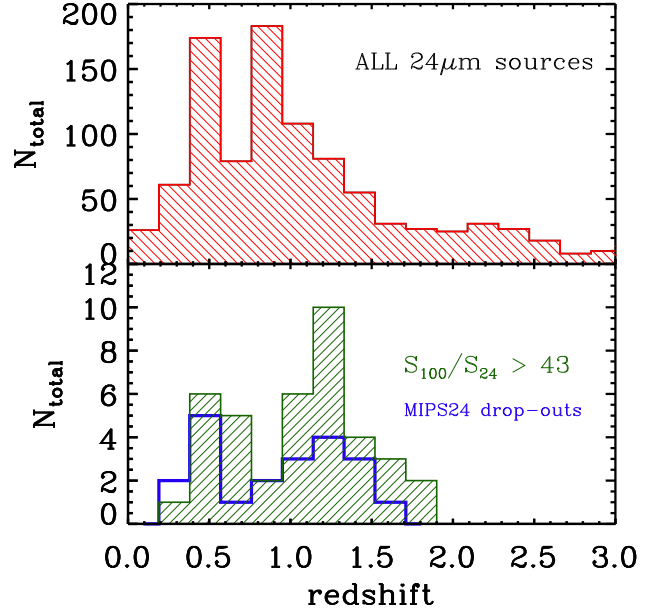


Fig. 7. Top: Redshift distribution of sources in GOODS-N with PACS 100 μm and MIPS 24 μm detections. Bottom: Redshift distribution of sources in GOODS-N with $S_{100}/S_{24} > 43$. Sources are clustered around $z = 0.4$ and $z = 1.3$. The blue histogram corresponds to the redshift distribution of MIPS dropouts.

galaxies”, attributing their blue S_{16}/S_{24} colour to the existence of a strong silicate absorption feature at 9.7 μm . This approach had two main caveats. First, the blue S_{16}/S_{24} colour is not necessarily produced by a silicate absorption feature, as similar colours can appear for sources with strong PAHs and low dust continuum. Second, many objects at lower redshifts fall within the same colour cut (Teplitz et al. 2005). A more recent attempt by Teplitz et al. (2011), reports that a higher ratio ($S_{16}/S_{24} > 1.4$), would eliminate many but not all of the low- z interlopers.

Here, we face the same situation. The cut in the S_{100}/S_{24} ratio that we have adopted selects sources in two redshift bins. In order to reject the low- z sources in our sample, simply increasing the S_{100}/S_{24} cut is not useful as apart from the low- z , we also miss many high- z sources and the selection is still not pure enough. Alternatively, we can employ a second colour criterion, based on the 16 μm and 8 μm flux densities. In Fig. 8 we plot the S_{100}/S_{24} vs S_{16}/S_8 colour – colour diagram for sources that have a 16- and 8 μm detection. We see that if a ratio cut of $S_{16}/S_8 > 4$ is combined with a S_{100}/S_{24} cut > 43 , then we successfully reject all low- z interlopers, while selecting sources in the $1.0 < z < 1.7$ redshift bin. The selection of S_{16}/S_8 as a second colour criterion was driven by the fact that at $1.0 < z < 1.7$ the 16 μm band probes the PAH complex (6.2 – 7.7 μm), boosting the value of S_{16} while for the low redshift sources only traces emission from a warm dust continuum at $> 10 \mu\text{m}$. We note that none of our sources is classified as an AGN, based on their X-ray emission, their optical spectra or their mid-IR colours (i.e. power law AGNs). It therefore seems that we have found a way to select star-forming high- z galaxies in a narrow redshift bin. In what follows we argue that these sources are compact starbursts with moderate/strong silicate features in their MIR spectrum.

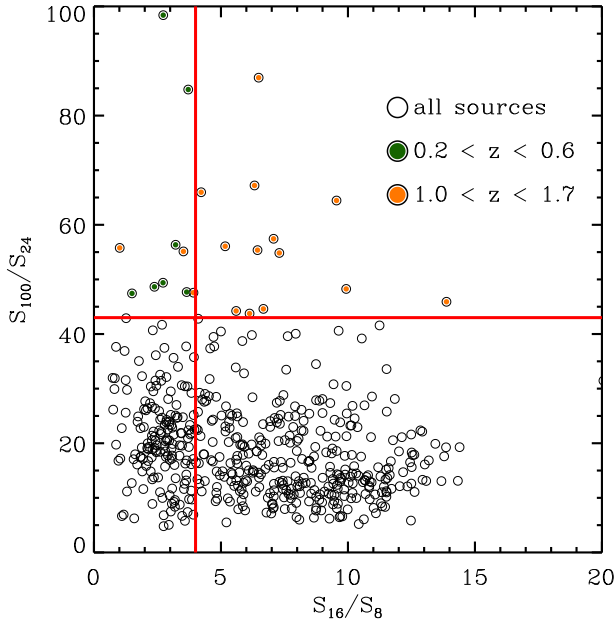


Fig. 8. S_{100}/S_{24} vs S_{16}/S_8 colour – colour diagram for the whole GOODS-H sample in GOODS-N with 16 μ m detection (black circles). Circles filled with green and orange colour are sources with $S_{100}/S_{24} > 43$ at $0.2 < z < 0.6$ and $1.0 < z < 1.7$, respectively. Vertical and horizontal red lines indicate a cut off ratio of $S_{16}/S_8 > 4$ and $S_{100}/S_{24} > 43$. We see that this diagram can serve as a redshift diagnostic, for sources at $1.0 < z < 1.7$.

4.2. Evidence for silicate absorption

We have already discussed in the Introduction, that for normal galaxies, i.e. those with $L_{\text{IR}} < 10^{10} L_{\odot}$, discriminating between moderate PAH emission superposed on a silicate-absorbed continuum and strong PAH features with a relatively weak underlying continuum is a difficult task (e.g. Smith et al. 2007), even when high quality mid-IR spectra are available. A typical example is M82, for which Sturm et al. (2000) suggests that there is no silicate absorption since the 10 μ m dip can be reproduced by a superposition of strong PAHs and VSG continuum. On the other hand, things are more straightforward for more luminous infrared sources, where there is clear evidence for the existence of a wide range of silicate optical depths, both for local and high- z LIRGs and ULIRGs (Armus et al. 2007, Pereira-Santaella et al. 2010). Unlike the sample based on the blue S_{16}/S_{24} colour, for which the L_{IR} estimates were based on large/uncertain extrapolations, our study benefits from more robust *Herschel*-based L_{IR} estimates. The fact that all sources with $S_{100}/S_{24} > 43$ at $1.0 < z < 1.7$ in our sample (including the high- z 24 μ m dropouts) have $L_{\text{IR}} > 10^{11} L_{\odot}$, coupled with the lack of observational evidence of sources with similar luminosities and low dust continuum emission, is a first hint that these sources have a silicate absorption feature at 9.7 μ m.

We have already demonstrated in Fig. 4, that these sources have S_{100}/S_{24} colours consistent with those of local templates of LIRGs and ULIRGs with moderate/high silicate strength. To further investigate this, we plot the distribution of the S_{100}/S_{24} colour of the GOODS-H (GOODS-N and GOODS-S) sources with spectroscopic redshift at $1.0 < z < 1.7$, along with the range of the S_{100}/S_{24} colour at this redshift range for 5 LIRG/ULIRG observed templates with a wide range of $\tau_{9.7}$ values (Fig. 9). In practice, this plot examines the detailed distribution of galaxies in the $1.0 < z < 1.7$ region of Fig. 4. Fitting the

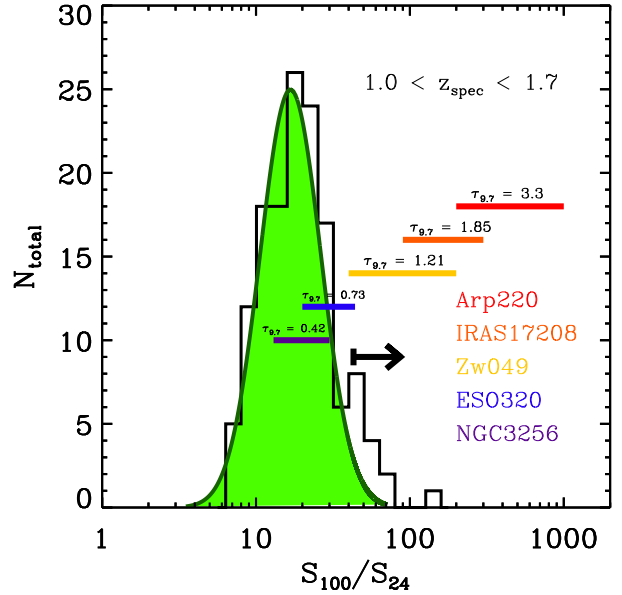


Fig. 9. Distribution of the S_{100}/S_{24} colour among sources in the GOODS-H sample with spectroscopic redshift at $1.0 < z < 1.7$. Green line and green shadowed area indicates the Gaussian fit to the distribution and the area beneath it. Coloured bars indicate the range of the S_{100}/S_{24} colour of several observed SEDs of local LIRGs and ULIRGs at this redshift bin. The silicate optical depths of the local sources, as derived by IRS spectroscopy are also overlaid. The black arrow indicates the position of the high- z 24 μ m dropout sample.

colour distribution with a Gaussian indicates a clear excess in the red tail due to sources with $S_{100}/S_{24} > 43$. It is crucial to stress that this excess is absent in other redshifts bins. Furthermore, we see that based on the template SEDs, sources with higher optical depth exhibit redder S_{100}/S_{24} colours in this redshift bin. In other words, it seems that the S_{100}/S_{24} colour could serve as a rough indicator of the silicate strength. Our sources, i.e. those with $S_{100}/S_{24} > 43$, have colours consistent with $0.7 < \tau_{9.7} < 1.9$, while it appears that none of them have a silicate feature as strong as that of Arp220. We note however, that we cannot rule out a source in our sample with stronger silicate but colder T_{dust} .

An alternative explanation of the high S_{100}/S_{24} ratios of these sources would be enhanced 100 μ m emission, simply because the sources are warmer, and hence their SEDs peak at shorter wavelengths. To test this, we investigate the S_{100}/S_{24} colour as a function of dust temperature, as indicated by the S_{160}/S_{100} ratio. In Fig. 10, we present this colour–colour diagram for sources at $1.0 < z < 1.7$, which are detected at 160- and 100 μ m. It appears that the adopted S_{100}/S_{24} cut does not introduce a bias towards warmer sources (i.e. sources with low S_{160}/S_{100} colours), as it selects sources with a wide range of dust temperatures similar to that found for the whole GOODS-H sample in this redshift bin, suggesting that an enhanced S_{100} is not the main reason for their high S_{100}/S_{24} ratios. We note that a large dispersion of dust temperature of high- z galaxies has recently been demonstrated by Hwang et al. (2010) and Magdis et al. (2010d).

One of the sources that meets the selection criteria is the well studied sub-millimetre source at $z = 1.21$, GN26 for which Pope et al. (2008) have published an IRS spectrum. The detection of this source in the PACS bands has also been discussed by Dannerbauer et al. (2010) and Magnelli et al. (2010) while Frayer et al. (2008) has reported the detection of CO(2 \rightarrow 1) emis-

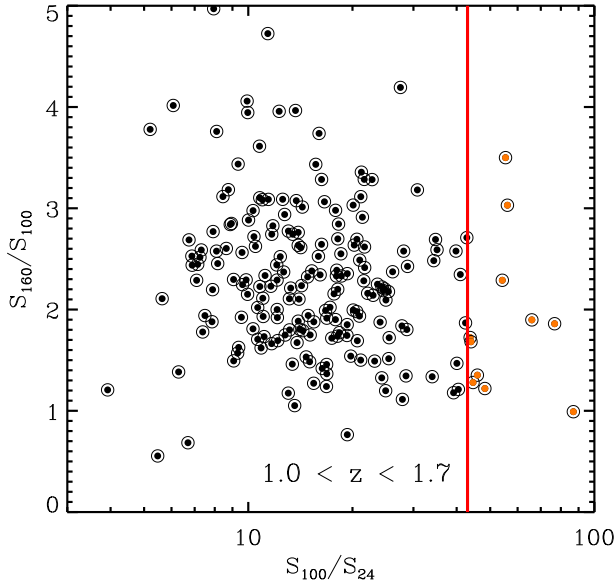


Fig. 10. S_{160}/S_{100} vs S_{100}/S_{24} colour – colour diagram for sources in the GOODS-H sample at $1.0 < z < 1.7$. Sources with $S_{100}/S_{24} > 43$ and $S_{16}/S_8 > 4$ are filled with orange colour. This plot demonstrates that our selection is not biased towards warmer sources.

sion. In Fig. 11, we show the full SED of the source, overlaid with the best CE01 template for the far-IR part and the observed IRS spectrum for the mid-IR part of the SED. The IRS spectrum of GN26 is also presented separately in an inset panel. This source has $S_{100}/S_{24} \sim 70$, and according to Fig. 9, it should have a silicate optical depth of ~ 1 . Although the S/N of the IRS spectrum does not allow for a robust measurement of $\tau_{9.7}$, its IRS spectrum is very similar to that of the composite spectrum of SMGs presented in Pope et al. (2008), and for which they report $\tau_{9.7} \sim 1$ in excellent agreement with what we expected based on this source’s S_{100}/S_{24} colour. We should also note that GN26 was one of the 13 sources used for the construction of the composite spectrum. Taken together, the evidence suggests that the red S_{100}/S_{24} colour of our sample is caused by the existence of a moderate/strong silicate absorption feature at $9.7 \mu\text{m}$, that enters the $24 \mu\text{m}$ band at these redshifts. We therefore choose to characterize these sources as *silicate-absorbed* galaxies.

4.3. The far-IR properties of the high- z sample

In the pre-*Herschel* era the far-IR properties of large samples of galaxies were derived based on large extrapolations of their $24 \mu\text{m}$ flux density using SED templates based on local IR-luminous galaxies. Recent studies using *Herschel* data have confirmed the validity of these extrapolations, demonstrating that the $24 \mu\text{m}$ flux density is a good proxy of the total L_{IR} , at least up to $z \sim 1.5$ (Elbaz et al. 2010). On the other hand, here we have found a population of high- z sources ($1.0 < z < 1.7$), that exhibit atypically red S_{100}/S_{24} colours. For these sources, we expect that L_{IR} estimates based on their S_{24} , and using average template SEDs, such as CE01 and DH02, would be severely underestimated.

In Fig. 12 we plot the S_{100}/S_{24} colour of all GOODS-H galaxies as a function of the ratio between the *Herschel* based L_{IR} and the one derived using only the $24 \mu\text{m}$ flux density. Although for the majority of the sources the two L_{IR} estimates are in good agreement (within a factor of ~ 1.5), for the high- z sources with $S_{100}/S_{24} > 43$ the $24 \mu\text{m}$ flux density would un-

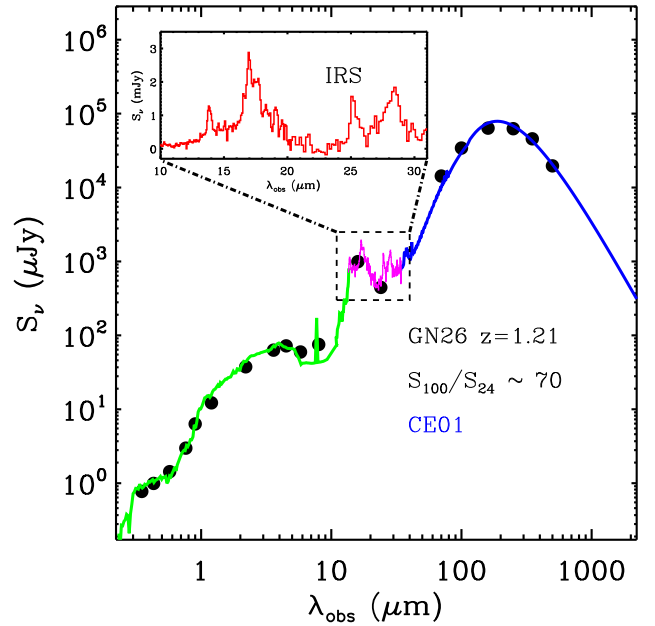


Fig. 11. Full SED of GN26, a source at $z = 1.21$ with $S_{100}/S_{24} \sim 70$. The far-IR part of the SED is derived from *Herschel* data and is overlaid with the best fit CE01 model. The mid-IR part of the SED is the observed IRS spectrum from Pope et al. (2008), that is also presented separately in the inset figure. We also show the optical/near-IR part of the SED along with the best fit BC03 model.

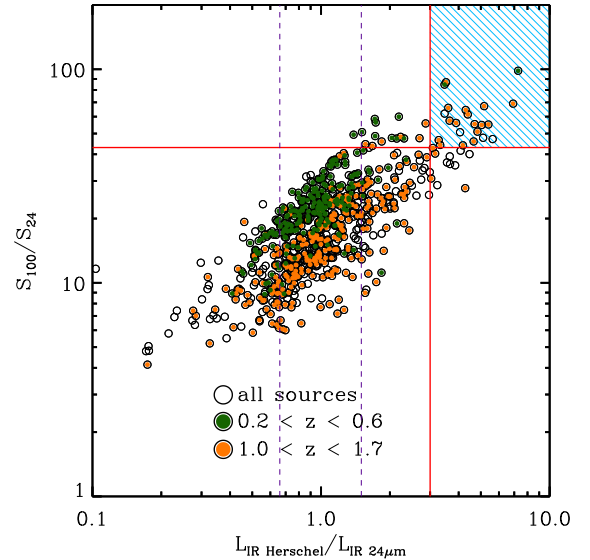


Fig. 12. S_{100}/S_{24} as a function of the *Herschel* derived L_{IR} over the L_{IR} derived based only on the $24 \mu\text{m}$ flux densities. Green circles are sources at $0.2 < z < 0.6$ and orange circles are sources at $1.0 < z < 1.7$. The top right box (defined by $S_{100}/S_{24} > 43$ and $L_{\text{IR}}^{\text{Herschel}} / L_{\text{IR}}^{24\mu\text{m}} > 3$) consists mainly of sources at $1.0 < z < 1.7$. Vertical dashed lines indicate the area where the two L_{IR} estimates agree within a factor of 1.5.

derestimate the true L_{IR} on average by a factor of > 3 . This is not the case for the low- z sample where the two estimates are in better agreement. For the high- z sample there is a clear trend between the S_{100}/S_{24} colour and the ratio of the two L_{IR} estimates, in the sense that the true L_{IR} is progressively underestimated for sources with redder S_{100}/S_{24} colours, depicting the limited variety of SEDs used for the derivation of the L_{IR} . This indicates

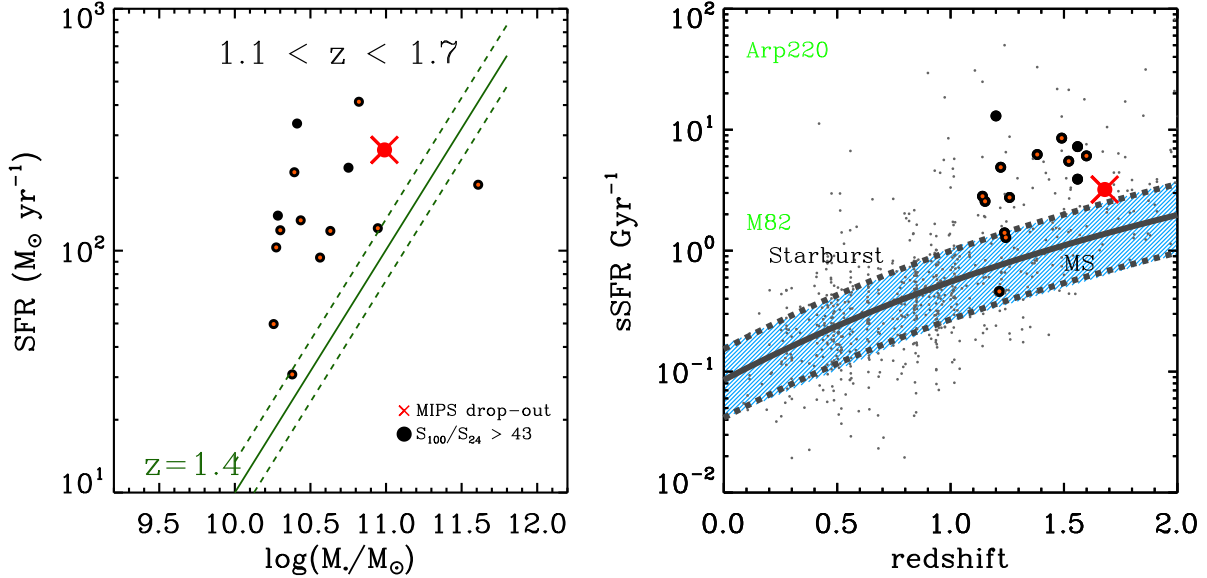


Fig. 13. Left: The SFR – M_* relation for sources with $S_{100}/S_{24} > 43$ at $1.1 < z < 1.7$ (black circles). Orange dots indicate sources with spectroscopic redshift. Red cross corresponds to the ULIRG dropout that we presented in Section 3.3. The solid green line depicts the SFR– M_* correlation at $z \sim 1.4$ (Elbaz et al. 2011), while the dashed lines indicate its dispersion. Right: Specific star formation rate (sSFR), as a function of redshift, for the same sample as in the left panel, as well as for the whole GOODS-H sample (grey dots). The gray thick line denotes the evolution of the sSFR with redshift, as derived by individual detections and stacking analysis of the GOODS-H sample by Elbaz et al. (2011). The blue shaded area along with the dashed gray lines which correspond to the dispersion of the evolution (~ 0.3 dex), indicate the region of main sequence galaxies. Sources with $S_{100}/S_{24} > 43$ tend to be found above the blue shaded area, populating the starburst region. The green text indicates the position of Arp 220 and M82 (shifted to $z = 0.1$ for clarity)

that although the average template SEDs are representative for the bulk of the galaxy population at $z < 1.5$, this is not the case for a population at $1.0 < z < 1.7$ with very red S_{100}/S_{24} colours (> 43 for this study).

4.4. The starburst nature of the high- z sample

As the silicate absorption feature merely requires a mass of warm dust obscured by a significant column of cooler dust, it does not provide any insight into the mechanism that is heating the warm dust. Hence, it is difficult to establish a correlation between the strength of this feature and the source that powers the mid-IR emission of infrared luminous galaxies, as it could equally be produced by a deeply buried AGN or a compact starburst (Farrah et al. 2008, Imanishi et al. 2009, Armus et al. 2007).

We have already reported that none of our sources show direct signs of AGN activity, since none of them are either (a) detected in X-rays in the 2 Msec Chandra observations (Alexander et al. 2003), (b) satisfies the criteria of power-law AGN or (c) has high excitation lines in their optical spectra (where available). A deeply obscured AGN though, cannot be ruled out. To investigate this, we stack the Chandra X-ray data on these sources. We find a strong detection (7σ) in the 0.5–2 keV band corresponding to $L_{2-10} = 3 \times 10^{41} \text{ erg sec}^{-1}$ and no detection in the 2–7 keV band (3σ upper limit $1.28 \times 10^{-17} \text{ erg cm}^{-2} \text{ s}^{-1}$). The derived upper limit in the hard band along the stacking results in the soft band suggest that the sources are dominated by star formation (Nandra et al. 2002, Lehmer et al. 2008). Furthermore, in most cases the radio based L_{IR} is in good agreement with that derived by *Herschel*, again indicating that those sources are dominated by a nuclear starburst, rather than an AGN.

It has recently been shown that normal star-forming galaxies exhibit a correlation between their SFR and stellar mass at

any given redshift. This correlation was first found among $z \sim 0$ galaxies (Brinchmann et al. 2004) and was subsequently extended to higher redshifts, $z \sim 1$ Elbaz et al. (2007), Noeske et al. (2007), $z \sim 2$ Daddi et al. (2007), Pannella et al. (2009), $z \sim 3$ Magdis et al. (2010a,b,c) and $z \sim 4$ Daddi et al. (2009). It has also been shown that star forming galaxies that do not follow this correlation tend to undergo a rapid starburst phase and have more compact geometries (Elbaz et al. 2011). For instance, at $z \sim 0$ and $z \sim 2$, respectively, local ULIRGs and SMGs have SFRs that greatly exceed the SFR– M_* correlation. Both classes of objects are thought to host compact starbursts (Daddi et al. 2010, Tacconi et al. 2010). It would therefore be interesting to investigate the position of the sources with red S_{100}/S_{24} colour in the SFR – M_* diagram. Using the Kennicutt 1998 relation and a Salpeter IMF, we convert the *Herschel* based L_{IR} to SFR for the sources with $S_{100}/S_{24} > 43$ and $1.1 < z < 1.7$ and we plot the derived SFR versus the stellar mass of the galaxies (Fig. 13, left). We also overplot the SFR– M_* correlation at the median redshift of the sample i.e., $z = 1.4$ (Elbaz et al. 2011). Clearly the sources are off the correlation, exhibiting enhanced star formation activity for their stellar mass. Similarly the ULIRG dropout source that we presented in section 3.3 is also off the correlation. To eliminate the effect of the evolution of the SFR– M_* with redshift, we also show the specific star formation rate (sSFR), defined as SFR/M_* , as function of redshift for sources with $S_{100}/S_{24} > 43$, as well as for the whole GOODS-H sample (Fig. 13, right). We also overplot the evolution of sSFR with time as derived by Elbaz et al. (2011), based both on detected sources and stacking analysis of the GOODS-H sample. According to Elbaz et al. (2011), sources within the blue shaded area are main sequence, normal star forming galaxies while sources above it, are considered to undergo a starburst phase. We find that sources with $S_{100}/S_{24} > 43$ tend to

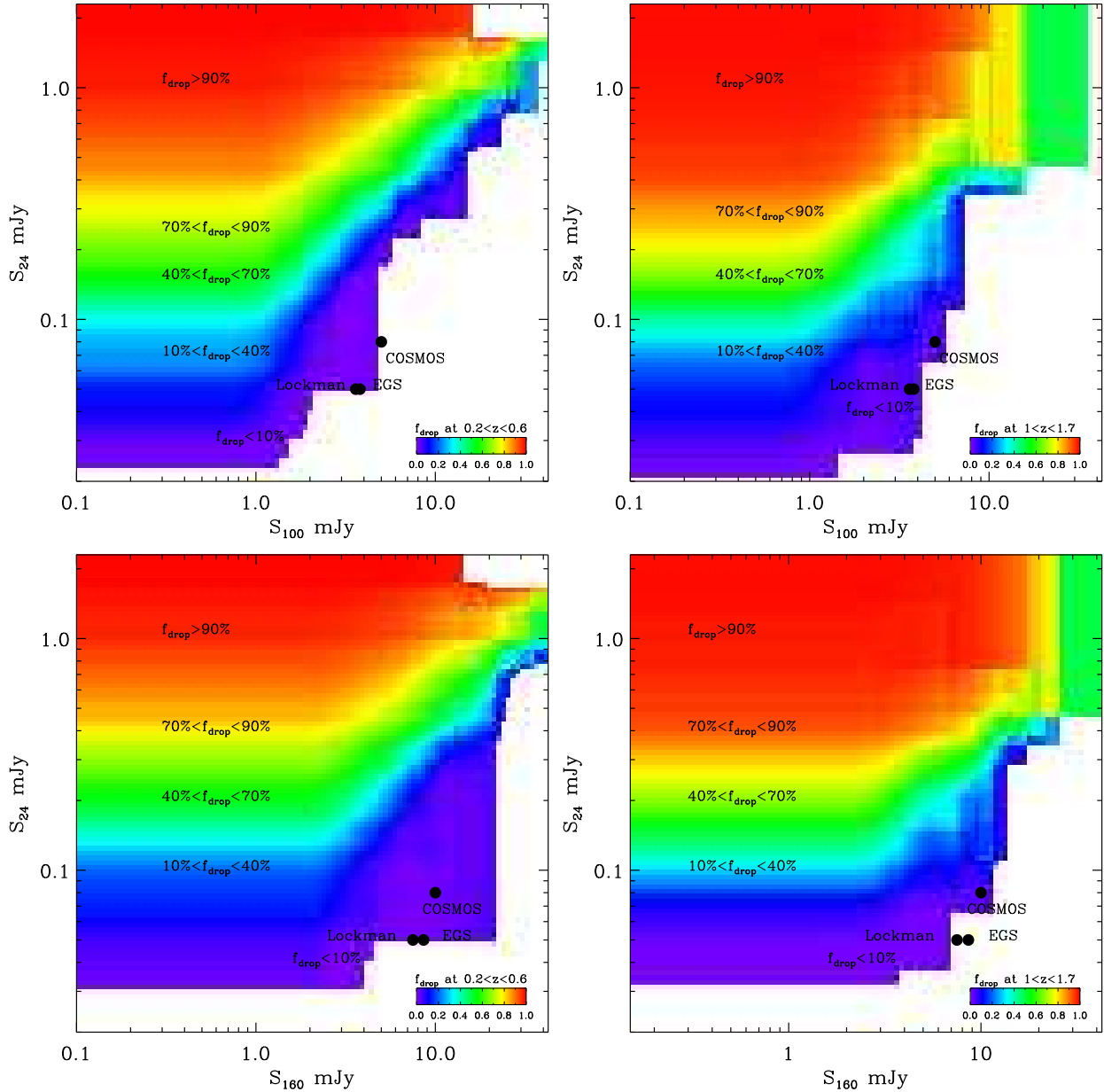


Fig. 14. The fraction of sources expected to be missed in the 24 μm band at $0.2 < z < 0.6$ (left) and $1.0 < z < 1.7$ (right) as a function of the 24 μm vs 100 μm (top) and the 24 μm vs 160 μm (bottom) depths. Black circles indicate the depths of PACS and MIPS 24 μm surveys for some of the most important cosmological fields, i.e. EGS, Lockman and COSMOS. We note that the region where the constant fraction isocontours run horizontally, cannot be constrained by the data. The adopted detection limits (5σ) at 24 μm are 80 μJy for COSMOS and 50 μJy for EGS and Lockman. Similarly the 3σ detection limits at 100 μm are 5.0-, 3.8- and 3.6 mJy (COSMOS, EGS and Lockman), while at 160 μm are 10.2-, 8.6- and 7.5 mJy.

have higher specific star formation rates when compared to main sequence star forming galaxies at this redshift range, and populate the starbursts region. This result is coherent with the picture where these sources are compact starbursts with high sSFR and where (like local ULIRGs) a strong silicate absorption feature at 9.7 μm is present in their mid-IR spectra.

5. Discussion

Previous studies predicted that the number of such silicate break sources could reach ~ 900 to 1500 sources per square degree, depending on the assumed model (e.g. Tagagi & Pearson 2005). Furthermore, Kasliwal et al. (2005), based on 16 μm IRS data, reported that such sources account for more than half of all

galaxies at $z \sim 1-2$ predicted by various models. The samples of silicate-break galaxies and MIPS dropout sources that we have found here can place strong limits on the number of $1.0 < z < 2.0$ infrared luminous galaxies with similar properties.

In the 250 arcmin² covered by PACS in the two GOODS fields, we have detected ~ 30 (7) silicate absorbed candidates at $1.0 < z < 2.0$ with $S_{100}/S_{24} > 43$ and $L_{\text{IR}} > 10^{11} L_{\odot}$ ($L_{\text{IR}} > 10^{12} L_{\odot}$). Assuming that all sources with $S_{100}/S_{24} > 43$ at this redshift are silicate absorbed starbursts, and neglecting the effects of cosmic variance, this implies a surface density of ~ 540 (220) sources deg⁻², significantly lower than previous predictions. Using the co-moving volume within $1 < z < 2$, this implies a space density of Si absorbed ULIRGs in this redshift bin of $\sim 2.0 (\pm 0.3) \times 10^{-5}$ Mpc⁻³. Comparing the numbers with

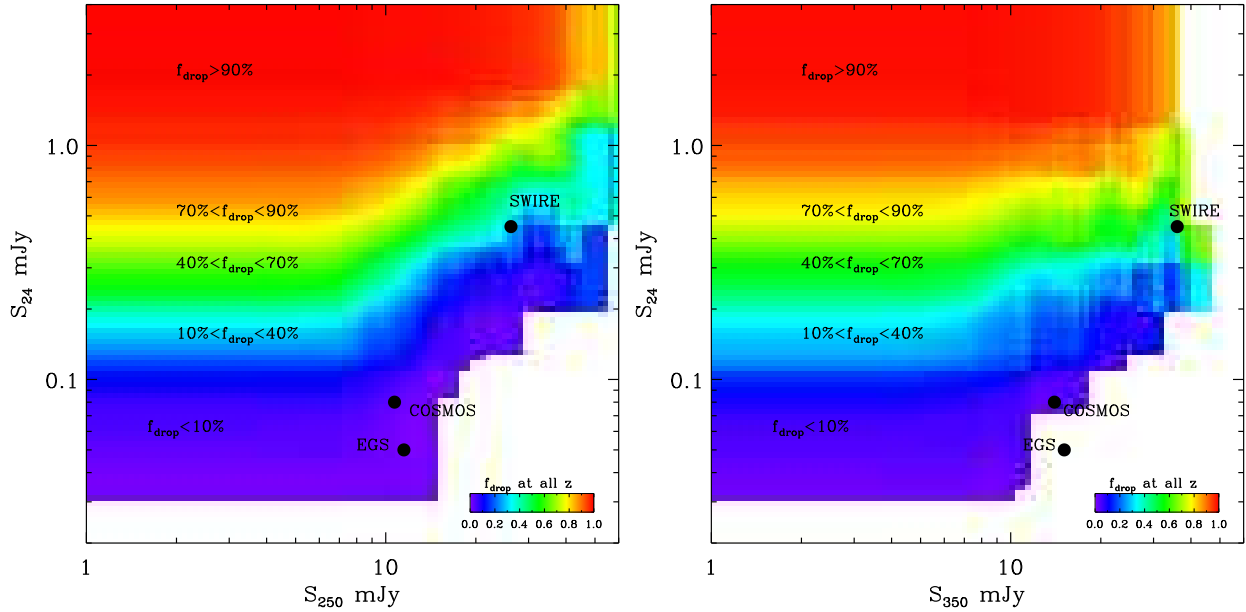


Fig. 15. The fraction of sources expected to be missed by the 24 μ m band at all redshifts as a function of the 24 μ m vs 250 μ m and the 24 μ m vs 350 μ m depth. Black circles indicate the depths of PACS and MIPS 24 μ m surveys for some of the most important cosmological fields, i.e. EGS, SWIRE and COSMOS.

the rest high- z sample of GOODS-H, we find that these sources account for the $\sim 8\%$ and 16% of the $L_{\text{IR}} > 10^{11} L_{\odot}$ and $L_{\text{IR}} > 10^{12} L_{\odot}$ sources at $1.0 < z < 2.0$. We note though, that our sample is not complete. As illustrated in Fig. 9, sources with silicate absorption feature but cold T_{dust} have $S_{100}/S_{24} < 43$ and are missed from the selection. We therefore conclude that this estimate is a rather conservative lower limit. Moving to the dropout sample, we have identified 11 sources with $L_{\text{IR}} > 10^{11} L_{\odot}$, accounting for approximately 1–2% of the population of $1 < z < 2$ infrared luminous galaxies in GOODS-H as a whole. We note that by comparing to the whole GOODS-H sample in the same redshift range, all effects of incompleteness are taken into account. Finally, these number should be treated as upper limits, given that some of these could be spurious detections, as discussed in Section 2.

These estimates confirm that for the GOODS surveys, 24 μ m observations recover the vast majority of $z < 2$ sources and do not introduce a strong selection bias. Furthermore, we confirm that using the 24 μ m catalogues to define priors for the extraction of PACS sources should only miss a small fraction of high- z sources. Of course the ratio between the number of sources missed by the 24 μ m band and the total number of sources in the PACS bands strongly depends on the depth of the MIPS 24 μ m and PACS observations. This is illustrated in Fig. 14, where we show the fraction of the expected dropouts at $0.2 < z < 0.6$ and $1.0 < z < 1.7$ as a function of the 24- to 100 μ m and the 24- to 160 μ m depth. These estimates are solely based on observations (i.e. on the GOODS-H sample), without any further assumptions. We simply calculate the ratio of f_{drop} :

$$\frac{\text{number of sources with } S_{100} > \alpha \text{ \& } S_{24} < \beta}{\text{number of sources with } S_{100} > \alpha \text{ \& } S_{24} > \beta}$$

where α and β are free parameters. These diagrams can be used as diagnostic of the fraction of sources that will be missed by a source extraction method based on 24 μ m priors for several extragalactic *Herschel* surveys, e.g. PEP (Lutz et al. 2011), HerMES (Oliver et al. in prep). We conclude that for the ma-

ior extragalactic surveys, there is not a large population of silicate break galaxies that would have been undetected in 24 μ m *Spitzer* data as some authors have previously suggested. This discrepancy could be indicative of an evolution of the strength of the silicate absorption feature with time. If the silicate features were weaker in early galaxies due to more extended star forming regions, then theoretical models based on local templates would grossly overestimate the number density of such sources. This scenario is in line with recent findings, where the star formation activity of the majority of high- z galaxies (including those with high L_{IR}), is similar to that of local spiral galaxies (e.g. Daddi et al. 2010, Genzel et al. 2010).

Finally, although in this work we have mainly focused on PACS data, it is worth attempting to quantify the fraction of sources that would be missed by a 24 μ m prior based source extraction in the SPIRE bands. The philosophy behind Fig. 15 is identical to that of Fig. 14, but this time considering the whole redshift range of the sources and the S_{250} (left) and S_{350} (right) flux density limits. We note that these detection limits, indicate the expected instrumental noise and do not take into account the confusion noise, which is dominant in the SPIRE bands.

6. Conclusions

We have presented a study dedicated to sources that exhibit atypical S_{100}/S_{24} colours using the deepest PACS data to date, obtained as part of the GOODS-H program. By performing blind source extraction we searched for sources that are bright in the far-IR but undetected at 24 μ m, i.e. for 24 μ m dropout galaxies. Then we investigated the properties of sources in the GOODS-H sample with red S_{100}/S_{24} colours searching for the population of silicate-break galaxies. The main results are summarized below:

- We have identified 21 PACS sources that are undetected at 24 μ m (down to a 3σ detection limit of $\sim 20 \mu\text{Jy}$). These 24 μ m dropout sources are found to have a bimodal redshift distribution, with peaks centred at $z \sim 0.4$ and ~ 1.3 , and are expected to exhibit strong silicate absorption features,

- responsible for their depressed 24 μ m emission. Among the sources in higher redshift we identify 10 LIRGs and one ULIRG at $z = 1.68$. This enables us to place upper limits in the fraction of LIRGs/ULIRGs that are missed by 24 μ m surveys.
- The vast majority of *Herschel* PACS sources are detected at 24 μ m, indicating that a prior-based source extraction based on the 24 μ m emission of the galaxies suffers only very modest incompleteness, with MIPS dropout sources accounting only for $\sim 2\%$ of the infrared luminous population in the GOODS fields. Although this fraction is negligible for the GOODS surveys, 24 μ m dropouts may be a concern for other *Herschel* extragalactic surveys with shallower 24 μ m data.
 - Based on the mid- and far-IR colours of sources in the GOODS-H sample, we demonstrated that sources with $S_{100}/S_{24} > 43$ and $S_{16}/S_8 > 4$ are located in a narrow redshift bin, $1.0 < z < 1.7$. Furthermore, we provided evidence that sources selected in this manner are starburst-dominated and with compact geometries. Similarly to the dropouts, the red S_{100}/S_{24} colours of these sources are attributed to the 9.7 μ m silicate absorption feature in their mid-IR spectra that enters into the 24 μ m band. We characterize them as silicate-absorbed galaxies.
 - The infrared luminosity of these silicate-absorbed galaxies, when derived based on their monochromatic 24 μ m flux density, is on average underestimated by a factor ~ 3 . They account for about 16% of the ULIRGs in the GOODS fields with a space density of $2.0 \times 10^{-5} \text{ Mpc}^{-3}$.
 - We provide diagnostic diagrams to estimate the fraction of sources expected to be missed in the 24 μ m band for several *Herschel* extragalactic surveys, and predict that for most of them that fraction is less than 10%.

Acknowledgements. G.E.M. acknowledge the support of the Centre National de la Recherche Scientifique (CNRS) and the University of Oxford. H.S.H and D.E. acknowledge the support of the Centre National d'Etudes Spatiales (CNES) PACS has been developed by a consortium of institutes led by MPE (Germany) and including UVIE (Austria); KU Leuven, CSL, IMEC (Belgium); CEA, LAM (France); MPIA (Germany); INAF/IFSI/OAA/OAP/OAT, LENS, SISSA (Italy) and IAC (Spain). This development has been supported by the funding agencies BMVIT (Austria), ESA-PRODEX (Belgium), CEA/CNES (France), DLR (Germany), ASI/INAF (Italy), and CICYT/MCYT (Spain). SPIRE has been developed by a consortium of institutes led by Cardiff University (UK) and including Univ. Lethbridge (Canada); NAOC (China); CEA, LAM (France); IFSI, Univ. Padova (Italy); IAC (Spain); SNSB (Sweden); Imperial College London, RAL, UCL-MSSL, UKATC, Univ. Sussex (UK); and Caltech, JPL, NHSC, Univ. Colorado (USA). This development has been supported by national funding agencies: CSA (Canada); NAOC (China); CEA, CNES, CNRS (France); ASI (Italy); MCINN (Spain); Stockholm Observatory (Sweden); STFC (UK); and NASA (USA). This work is based [in part] on observations made with *Herschel*, a European Space Agency Cornerstone Mission with significant participation by NASA. Support for this work was provided by NASA through an award issued by JPL/Caltech.

References

- Armus, L., Charmandaris, V., Bernard-Salas, J., et al. 2007, *ApJ*, 656, 148
 Ashman, K. M., Bird, C. M., & Zepf, S. E. 1994, *AJ*, 108, 2348
 Blain, A. W., Smail, I., Ivison, R. J., & Kneib, J. 1999, *MNRAS*, 302, 632
 Brandl, B. R., Bernard-Salas, J., Spoon, H. W. W., et al. 2006, *ApJ*, 653, 1129
 Brinchmann, J., Charlot, S., White, S. D. M., et al. 2004, *MNRAS*, 351, 1151
 Caputi, K. I., Lagache, G., Yan, L., et al. 2007, *ApJ*, 660, 97
 Charmandaris, V., Uchida, K. I., Weedman, D., et al. 2004, *ApJS*, 154, 142
 Chary, R. & Elbaz, D. 2001, *ApJ*, 556, 562
 Condon, J. J. 1992, *ARA&A*, 30, 575
 da Cunha, E., Charmandaris, V., Daz-Santos, T., et al. 2010, *A & A*, 523, A78
 Daddi, E., Dannerbauer, H., Stern, D., et al. 2009, *ApJ*, 694, 1517
 Daddi, E., Dickinson, M., Morrison, G., et al. 2007, *ApJ*, 670, 156
 Daddi, E., Elbaz, D., Walter, F., et al. 2010, *ApJ*, 714, L118
 Dale, D. A. & Helou, G. 2002, *ApJ*, 576, 159
 Dannerbauer, H., Daddi, E., Morrison, G. E., et al. 2010, *ApJ*, 720, L144
 Desai, V., Armus, L., Spoon, H. W. W., et al. 2007, *ApJ*, 669, 810
 Dickinson, M., Papovich, C., Ferguson, H. C., & Budavari, T. 2003, *ApJ*, 587, 25
 Diolaiti, E., Bendinelli, O., Bonaccini, D., et al. 2000, in *Astronomical Society of the Pacific Conference Series*, Vol. 216, *Astronomical Data Analysis Software and Systems IX*, ed. N. Manset, C. Veillet, & D. Crabtree, 623
 Dole, H., Gispert, R., Lagache, G., et al. 2001, *A&A*, 372, 364
 Elbaz, D., Cesarsky, C. J., Fadda, D., et al. 1999, *A&A*, 351, L37
 Elbaz, D., Daddi, E., Le Borgne, D., et al. 2007, *A&A*, 468, 33
 Elbaz, D., Dickinson, M., Hwang, H. S., et al. 2011, *ArXiv e-prints*
 Elbaz, D., Hwang, H. S., Magnelli, B., et al. 2010, *A&A*, 518, L29
 Farrah, D., Lonsdale, C. J., Weedman, D. W., et al. 2008, *ApJ*, 677, 957
 Frayer, D. T., Koda, J., Pope, A., et al. 2008, *ApJ*, 680, L21
 Giavalisco, M., Ferguson, H. C., Koekemoer, A. M., et al. 2004, *ApJ*, 600, L93
 Griffin, M. J., Abergel, A., Abreu, A., et al. 2010, *A&A*, 518, L3
 Higdon, S. J. U., Weedman, D., Higdon, J. L., et al. 2004, *ApJS*, 154, 174
 Houck, J. R., Roellig, T. L., van Cleve, J., et al. 2004, *ApJS*, 154, 18
 Houck, J. R., Soifer, B. T., Weedman, D., et al. 2005, *ApJ*, 622, L105
 Hwang, H. S., Elbaz, D., Magdis, G., et al. 2010, *MNRAS*, 409, 75
 Imanishi, M. 2009, *ApJ*, 694, 751
 Kasliwal, M. M., Charmandaris, V., Weedman, D., et al. 2005, *ApJ*, 634, L1
 Kennicutt, Jr., R. C. 1998, *ARA&A*, 36, 189
 Kim, D. & Sanders, D. B. 1998, *ApJS*, 119, 41
 Lagache, G., Dole, H., & Puget, J. 2003, *MNRAS*, 338, 555
 Le Floch, E., Papovich, C., Dole, H., et al. 2005, *ApJ*, 632, 169
 Lehmer, B. D., Brandt, W. N., Alexander, D. M., et al. 2008, *ApJ*, 681, 1163
 Lutz, D., Poglitsch, A., Altieri, B., et al. 2011, *ArXiv e-prints*
 Magdis, G. E., Elbaz, D., Daddi, E., et al. 2010a, *ApJ*, 714, 1740
 Magdis, G. E., Elbaz, D., Hwang, H. S., et al. 2010b, *MNRAS*, 409, 22
 Magdis, G. E., Elbaz, D., Hwang, H. S., et al. 2010c, *ApJ*, 720, L185
 Magdis, G. E., Rigopoulou, D., Huang, J., & Fazio, G. G. 2010d, *MNRAS*, 401, 1521
 Magnelli, B., Lutz, D., Berta, S., et al. 2010, *A&A*, 518, L28
 Nandra, K., Mushotzky, R. F., Arnaud, K., et al. 2002, *ApJ*, 576, 625
 Noeske, K. G., Weiner, B. J., Faber, S. M., et al. 2007, *ApJ*, 660, L43
 Pannella, M., Carilli, C. L., Daddi, E., et al. 2009, *ApJ*, 698, L116
 Papovich, C., Dole, H., Egami, E., et al. 2004, *ApJS*, 154, 70
 Pearson, C. P., Serjeant, S., Negrello, M., et al. 2010, *A&A*, 514, A9
 Pereira-Santaella, M., Alonso-Herrero, A., Rieke, G. H., et al. 2010, *ApJS*, 188, 447
 Pilbratt, G. L., Riedinger, J. R., Passvogel, T., et al. 2010, *A&A*, 518, L1
 Poglitsch, A., Waelkens, C., Geis, N., et al. 2010, *A&A*, 518, L2
 Pope, A., Chary, R., Alexander, D. M., et al. 2008, *ApJ*, 675, 1171
 Rieke, G. H., Alonso-Herrero, A., Weiner, B. J., et al. 2009, *ApJ*, 692, 556
 Sajina, A., Yan, L., Lacy, M., & Huynh, M. 2007, *ApJ*, 667, L17
 Serjeant, S., Efstathiou, A., Oliver, S., et al. 2001, *MNRAS*, 322, 262
 Smith, J. D. T., Draine, B. T., Dale, D. A., et al. 2007, *ApJ*, 656, 770
 Soifer, B. T. & Neugebauer, G. 1991, *AJ*, 101, 354
 Sturm, E., Lutz, D., Tran, D., et al. 2000, *A & A*, 358, 481
 Tacconi, L. J., Genzel, R., Neri, R., et al. 2010, *Nature*, 463, 781
 Takagi, T. & Pearson, C. P. 2005, *MNRAS*, 357, 165
 Teplitz, H. I., Charmandaris, V., Chary, R., et al. 2005, *ApJ*, 634, 128
 Teplitz, H. I., Chary, R., Elbaz, D., et al. 2011, *AJ*, 141, 1
 Werner, M. W., Roellig, T. L., Low, F. J., et al. 2004, *ApJS*, 154, 1